Research Square

Preprints are preliminary reports that have not undergone peer review.
They should not be considered conclusive, used to inform clinical practice,
or referenced by the media as validated information.

MoO_2-Coated Photonic Crystal Fiber Biosensor for High-Sensitivity Detection of Cancer Cells

Qi Zhai
Shanxi Datong University
Yang Zhang
Shanxi Datong University
Shuhuan Zhang
2692709482@qq.com

Beijing University of Technology
Yufan Sun
Shanxi Datong University
Jingqi Zhang
Shanxi Datong University
Siying Chen
Shanxi Datong University
Zuolong Li
Shanxi Datong University
Minghang Man
Shanxi Datong University
Xingyang Xu
Shanxi Datong University
Min Peng
Xinjiang Institute of Engineering
Yize Lu
Xinjiang Institute of Engineering
Jintao Wang
Xinjiang Institute of Engineering
Jiyu Dong
Shanxi Datong University

Research Article

Keywords: MoO2, Surface plasmon resonance, Cancerous cell, Photonic crystal fiber, Biosensing

Posted Date: August 18th, 2026

DOI: https://doi.org/10.21203/rs.3.rs-10426725/v1

License: This work is licensed under a Creative Commons Attribution 4.0 International License.
Read Full License

Additional Declarations: No competing interests reported.

MoO_2-Coated Photonic Crystal Fiber Biosensor for High-Sensitivity Detection of Cancer Cells

Qi Zhai[1], Yang Zhang[1*], Shuhuan Zhang[2,3*], Yufan Sun[1], Jingqi Zhang[1], Siying Chen[1], Zuolong Li[1], Minghang Man[1], Xingyang Xu[1], Min Peng[2], Yize Lu[2], Jintao Wang[2], Jiyu Dong[1]

1. College of Physics and Electronic Science, Shanxi Datong University, Datong 037009, China

2. Xinjiang Institute of Engineering, Urumqi 830023, China

3. Beijing Engineering Research Center of Laser Technology, Beijing University of Technology, Beijing, 100124, China

[*]Corresponding author: Yang Zhang E-mail: zhangyang@sxdtdx.edu.cn
Shuhuan Zhang 2692709482@qq.com

Abstract: A high-sensitivity surface plasmon resonance (SPR) biosensor based on a MoO_2-coated photonic crystal fiber (PCF) is proposed for cancer cell detection. Compared to conventional gold or silver films, the introduced MoO_2 coating offers superior environmental stability, with high resistance to oxidation and hydrolysis at room temperature. Its high free electron density in the valence band also enables strong SPR effects. The sensor's performance is numerically investigated using the finite element method (FEM). Through optimizing the fiber structure's key parameters—central air hole position, MoO_2 layer thickness and relative position of the top air hole, the sensor exhibits excellent sensing detection performance. Its maximum wavelength sensitivity reaches 17295.78 nm/RIU. The sensor can accurately distinguish six types of cancer cells, including Basal cells, cervical cancer HeLa cells, leukemia Jurkat cells, PC-12 cells, triple-negative breast cancer MDA-MB-231 cells, and breast cancer MCF-7 cells. Its corresponding wavelength sensitivity ranges from 15642 to 16750 nm/RIU. The resolution reaches 5.97×10^{-6} to 6.39×10^{-6} RIU. The newly designed sensor is able to recognize six distinct cancer cell variants. Meanwhile, it boasts promising application prospects in bioanalysis, clinical diagnosis, ecological surveillance and other relevant research fields.

Keywords: MoO_2; Surface plasmon resonance; Cancerous cell; Photonic crystal fiber; Biosensing

1. Introduction

Cancer has become a major disease that seriously endangers human health across the globe. Its incidence and mortality burdens keep increasing, posing severe challenges to public health and clinical diagnosis and treatment. In recent two years, relevant studies have generally pointed out that early diagnosis and timely intervention are key to improving cancer prognosis and enhancing patients' quality of life. They also serve as an important breakthrough in current tumor prevention and treatment. With the continuous development of diagnostic and therapeutic technologies, highly sensitive, non-invasive, rapid and reliable cellular and biochemical detection methods[1] have gradually become a research hotspot. However, traditional detection methods still show certain limitations in sensitivity, specificity or convenience. In this context, developing novel high-performance sensing and detection technologies carries significant research value and

application potential. It offers new solutions for early cancer screening and precise diagnosis. Commonly used clinical methods for cancer cell detection include blood tests, biopsy, magnetic resonance imaging (MRI) and positron emission tomography (PET) scanning[2]. Each of these methods has obvious limitations. They can hardly meet the demand for early and accurate detection.

Optical fiber sensing technology has developed rapidly. Photonic crystal fibers break through the limitations of traditional optical fibers owing to their unique periodic air-hole structure. They possess excellent optical properties such as flexible light confinement, endless single-mode transmission, high nonlinearity, and strong evanescent wave coupling[5]. These advantages provide a new route for biomedical sensing. PCF sensors can enhance the interaction between light and analytes by optimizing their air-hole structure and surface modification. They can accurately identify differences in refractive index and molecular characteristics between cancer cells and normal cells. Meanwhile, PCF sensors feature small size, resistance to electromagnetic interference and rapid detection[6]. They enable real-time in situ detection of cancer cells. These sensors effectively compensate for the drawbacks of traditional detection methods and have become a research hotspot in this field.

Over the past few years,researchers have designed multiple SPR-PCF sensing structures for monitoring biochemical substances. Existing research works have explored a wide spectrum designs, including various core geometries, various types of plasmonic metals, and different approaches for analyte injection. For example, Nagave[7]developed a dual-core biosensor capable of early cancer cell identification. The sensor is structured as a double-polished D-type configuration, where circular air holes are arranged into a hexagonal array. The polished region is covered with gold as the plasmonic layer. For this sensor, the wavelength sensitivities to MCF-7, MDA-MB-231, PC-12, HeLa, Jurkat and basal cancer cells are 5714.28, 4285.72, 4285.71, 3333.33 and 3000 nm/RIU, respectively. Its maximum resolution is 3.33×10^{-5} RIU. Ebrahimi et al. [8]proposed a high-sensitivity PCF-SPR biosensor. It adopts circularly arranged air holes and symmetric C-form grooves on either side of the PCF. The grooves are covered with graphene and gold thin films. Numerical analysis reveals that this sensor achieves the highest sensitivity for MCF-7 cells. It attains 2142.86 nm/RIU under spectral demodulation conditions. R. Kumar et al.[9] proposed a new SPR biosensor based on an Au-TiO_2 nanohybrid layer. The sensitivities for HeLa and MCF-7 cells are improved to 4078.43 and 4285.71 nm/RIU, respectively. The corresponding

resolution for basal cells reaches 4.0×10^{-5} RIU. Khodtarks Dashmian et al.[10]developed a highly sensitive SPR-PCF biosensor enhanced by gold nanowires. The fiber features air holes arranged in a hexagonal lattice. A U-shaped open channel is designed in the PCF for efficient analyte injection, with gold nanowires embedded inside. Numerical analysis reveals that the sensor exhibits the highest wavelength sensitivity for MCF-7 breast cancer cells. It reaches 7857.14 nm/RIU in the near-infrared region. This sensor enables label-free, high-throughput detection of multiple cancer cell types. Most conventional cancer diagnostic biosensors feature intricate structures and exhibit low detection performance in terms of wavelength sensitivity and spectral resolution. Hence, it is essential to develop a high-performance sensor with a simple structural layout.

A novel D-shaped PCF sensor based on the SPR principle is proposed in this paper for detecting various types of cancer cells. This sensor employs the metal oxide molybdenum dioxide (MoO_2) as the excitation material to distinguish six types of cancer cells: basal cells, HeLa cells, Jurkat cells, PC-12 cells, MDA-MB-231 cells, and MCF-7 cells. The functional performance of the designed sensor is verified via finite element method (FEM) simulations. The sensor's resolution was assessed as a key metric for characterizing its sensitivity to variations in cellular refractive index. The results demonstrate that this sensor possesses considerable potential for the rapid and precise identification of the six cancer cell types. It provides new technical support for early screening and precise diagnosis of cancer, and promotes the clinical translation and application of PCF sensing technology in biomedical diagnostics.

2. Structural Designand Numerical Analysis

A schematic of the sensor's two-dimensional cross-sectional geometry is presented in Fig. 1. The sensor's photonic crystal fiber consists of a silica background with an array of air holes featuring two distinct diameters. The inner and outer double-layer air holes are arranged in a hexagonal pattern. The diameter of the small inner and outer air holes is d_1=0.3 μm, and the large outer air holes have a diameter of d_2=0.5 μm. Large air holes confine optical energy within the fiber core. Small air holes control energy leakage from the core to the sensing region. The distance from the inner-layer air holes to the core center is Λ_2= 1.25 μm. The distance for the outer-layer air holes is Λ_3= 2.0 μm. The polishing depth is h_1= 1.6 μm. By offsetting the core, the design reduces the gap between the plasmonic layer and the optical core region. This allows light to leak more easily into the plasmonic layer and excite surface plasmon resonance. Compared with conventional coating methods, one side of the fiber is polished into a flat plane, and molybdenum

dioxide is deposited on this surface. This D-shaped structure facilitates material filling and coating modification, making the operation much simpler.

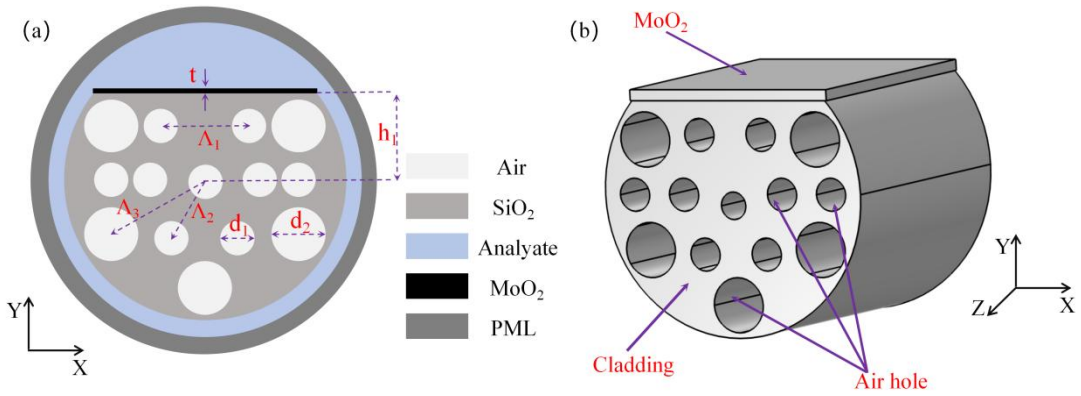


Fig. 1(a) Cross section of the proposed D-shaped MoO_2-coated PCF (b)Three-dimensional structural model of D-type optical fiber sensor

These air holes are embedded in the silica fiber substrate (SiO_2). The refractive index of silica can be obtained from the Sellmeier equation[11].

$$n^2 - 1 = \frac{A_1\lambda^2}{\lambda^2 - B_1^2} + \frac{A_2\lambda^2}{\lambda^2 - B_2^2} + \frac{A_3\lambda^2}{\lambda^2 - B_3^2} \tag{1}$$

Where λ represents the wavelength of incident light in the fiber. The other parameters in the formula are Sellmeier constants, which are given as:A_1 = 0.6961663, A_2 = 0.4079426, A_3 = 0.8974794,B_1 = 0.684043 μm, B_2 = 0.1162414 μm, B_3 = 9.896161 μm.

The Drude model is applied to characterize the dielectric function of MoO_2, which serves as the plasmonic material[12]. The Drude model is a well-established theoretical framework fundamental to describing the optical behavior of metallic and semiconductor materials. It is well-suited for modeling the electron dynamics and plasmon resonance in such materials.

$$\varepsilon_m = \varepsilon_\infty - \frac{\omega_p^2}{\omega(\omega + i\gamma)} \tag{2}$$

This study assumes a value of ε_∞=1. The value of this parameter represents the high-frequency permittivity of MoO_2. The parameters are defined as follows: ω_p is the plasma frequency and γ is the damping rate. In plasmon-supporting materials, the plasma frequency acts as the primary determinant of the resonant peak's spectral position. This frequency corresponds to the characteristic frequency of coherent electron oscillations in the material. The damping rate is the key factor dominating the broadening of the resonant peak. This parameter quantifies the energy loss associated with damped electron oscillations. The damping rate governs the

non-radiative decay lifetime of plasmons, which in turn dictates the extent of spectral broadening.

In addition, the confinement loss of the fiber can be expressed by the following formula[13]. Here, Im(neff) represents the imaginary part of the effective refractive index of the optical mode.

$$\alpha(x,y) = 8.686 \times \frac{2\pi}{\lambda} \mathrm{Im}[n_{eff}] \times 10^4 \tag{3}$$

As a key metric, spectral sensitivity is central to assessing the working characteristics of SPR-PCF based biosensing platforms. The spectral sensing characteristics of PCF-SPR sensors in cancer detection arises from the refractive index contrast between healthy and malignant cells, which induces a measurable resonance wavelength shift. It can be defined as[14], where $\Delta\lambda_{peak}$ represents the variation in resonance wavelength and Δn_a denotes the change in analyte refractive index.

$$S_\lambda(\lambda) = \frac{\Delta\lambda_{\mathrm{peak}}}{\Delta n_a} \tag{4}$$

Amplitude sensitivity is equally important as spectral sensitivity in sensor performance evaluation. The former can be expressed as[15], where $\alpha(\lambda, n_a)$ denotes the total loss, ∂n_a is the change in analyte refractive index, and $\partial\alpha(\lambda, n_a)$ represents the difference between two adjacent loss values at a given wavelength and refractive index.

$$S(RIU^{-1}) = -\frac{1}{\alpha(\lambda, n_a)} \frac{\partial\alpha(\lambda, n_a)}{\partial n_a} \tag{5}$$

The sensor resolution can be expressed as follows[16]:

$$R = \Delta n_a \frac{\Delta\lambda_{\mathrm{min}}}{\Delta\lambda_{peak}} \tag{6}$$

With a minimum spectral resolution of 0.1 nm, $\Delta\lambda_{peak}$ corresponds to the resonance wavelength deviation, while Δn_a signifies the variation in the analyte refractive index.

3. Results and Discussion

Fig. 2(a) shows the dispersion and confinement loss of the x- and y-polarized fundamental modes and the surface plasmon polariton (SPP) mode at an analyte refractive index of RI = 1.39. The solid red line and dashed red line represent the losses of the x- and y-polarized fundamental modes in the wavelength range of 1000-1800 nm, respectively. The dashed and solid blue lines show the real part of the effective refractive index for the x-polarized core mode and the SPP

mode, respectively, as a function of wavelength. The confinement loss of the x-polarized fundamental mode reaches a maximum of 4456.8 dB/cm at 1410 nm. A resonant coupling occurs at this specific wavelength, as the effective index of the fundamental core mode equals the real part of the SPP mode index, which is a prerequisite for efficient excitation. The phase-matching point is identified at the intersection of the two effective index dispersion curves, and its corresponding wavelength is defined as the resonance wavelength. The coupling strength between the fundamental mode and the surface plasmon polariton mode at this point critically determines the sensor's performance. Resonant coupling occurs at a wavelength of 1410 nm. Its corresponding effective refractive index is 1.3640. Electric field distributions exist near the molybdenum dioxide coating and the fiber core. It implies the occurrence of effective coupling between the basic mode and the SPP mode. The experimental setup of the proposed sensor is illustrated in Fig. 2(b). In the experimental setup, near-infrared light from the source is guided via an optical fiber to the SPR-PCF sensor. The near-infrared band was selected due to its superior tissue penetration depth and minimized scattering effects in biological media. Although certain challenges exist in the generation and detection of near-infrared light, this wavelength band selection can effectively improve the sensor's sensitivity in detecting cancerous cells. Commercial high-performance light sources and photodetectors are capable of satisfactorily overcoming these challenges. The analyte sample is placed in a reservoir and injected evenly into the SPR-PCF sensor, allowing full interaction with the optical field. Optical signals carrying analyte refractive index information are then delivered to an optical spectrum analyser. The data collected by the analyzer is transferred to a computer for subsequent processing and analysis.

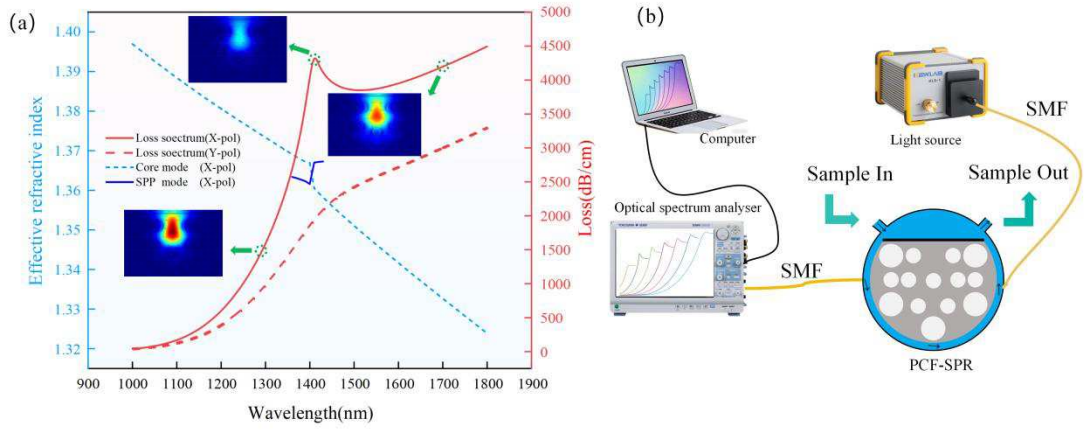


Fig. 2(a) X-polarized and Y-polarized core mode and SPP mode effective RI real part with the change of wavelength. Loss spectrum of y-polarized core mode of sensor. (b) the recommended experimental setup

Structural parameter variations significantly affect sensing performance. Three structural parameters are investigated for their sensing performance changes. Fig. 3(a–c) show the influence of different-thickness MoO_2 layers on confinement loss spectra at refractive indices from 1.35 to 1.41.For a fixed MoO_2 thickness, the resonant wavelength of the x-polarized mode blue-shifts as the refractive index increases. The loss intensity gradually decreases accordingly. At a thickness of 25 nm, the resonance wavelength blue-shifts from 2163.54 nm to approximately 1115.18 nm, while the loss intensity decreases from about 5838.596 dB/cm to approximately 3556.64 dB/cm. For a thickness of 30 nm, the resonance wavelength blue-shifts from about 2097.68 nm to around 1120.14 nm, and the loss reduces from roughly 5703.50 dB/cm to about 2731.57 dB/cm. When the thickness is 35 nm, the resonance wavelength blue-shifts from approximately 2045.57 nm to about 1117.55 nm, with the loss declining from around 5589.47 dB/cm to roughly 2203.51 dB/cm. As the thickness of MoO_2 increases from 25 nm to 35 nm, the resonance wavelength of the x-polarized core mode exhibits a slight blue shift at the same refractive index, and the resonance intensity decreases significantly. When the refractive index is 1.38, the resonance wavelength is approximately 1608.98 nm at 25 nm thickness, about 1573 nm at 30 nm, and around 1549.11 nm at 35 nm.At RI = 1.35, the peak loss is roughly 5854.39 dB/cm for 25 nm thickness, about 5698.49 dB/cm for 30 nm, and approximately 5591.22 dB/cm for 35 nm. As the coating thickness increases, a continuous dense film layer forms. This suppresses leakage of the evanescent field from the core-guided mode, interface scattering, and mode coupling loss, leading to a significant reduction in overall loss. Meanwhile, the increased coating thickness weakens the quantum size effect and modifies the dielectric properties of MoO_2, thereby lowering the effective refractive index of the surface plasmon polaritons. Combined with a slight decrease in the effective refractive index of the guided mode, this collectively induces a blue-shift of the resonance peak toward shorter wavelengths. Fig. 3(d) quantifies the sensor performance at different MoO_2 thicknesses. The linear fitting results between resonance wavelength and analyte refractive index show that at 25 nm thickness, the sensitivity is 17295.78 nm/RIU with a goodness-of-fit R^2 = 0.99854. At 30 nm thickness, the sensitivity is 16343.57 nm/RIU (R^2 = 0.99867). For 35 nm thickness, the sensitivity is 15449.64 nm/RIU (R^2 = 0.99870). The results indicate that reducing the MoO_2 thickness significantly enhances the sensor sensitivity, with a maximum achievable sensitivity of 17295.78 nm/RIU. Across all thicknesses, the linear fittings are excellent, with R^2 values all above 0.998, ensuring high accuracy and reliability in refractive index detection.

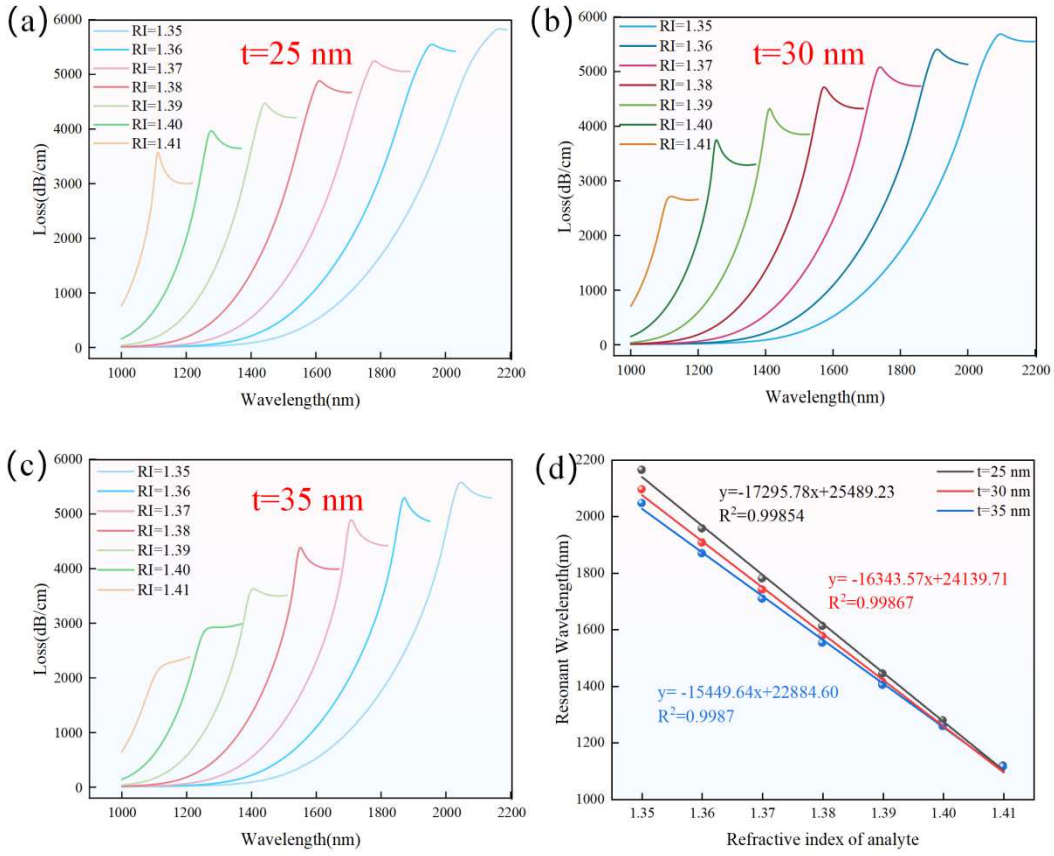


Fig. 3(a-c)the wavelength-dependent loss characteristics of the x-polarized core mode under the conditions of MoO_2 thicknesses of t = 25, 30, and 35 nm, respectively. (d) Linear fitting curves of effective RI versus resonant wavelength for x-polarized core modes under different MoO_2 thicknesses

Fig. 4(a–b) present the confinement loss, optical field energy density distributions and power flow directions of the D-type photonic crystal fiber. The central air hole is displaced upward by Δ = 0 to 1.3 μm, where Δ denotes the height difference between the final and initial positions relative to the center. The color gradient from blue to red represents the variation in energy density from low to high, while the red arrows indicate the direction of energy flow. At Δ = 0, the optical field in the y-polarization direction exhibits a "teardrop" shape and strongly concentrates toward the coated region on the D-shaped surface. The energy flow arrows point toward the coating surface. This indicates strong coupling between the guided mode and the surface plasmon mode. As a result, substantial optical energy leaks into the coating region. In contrast, the optical field in the x-polarization direction shows a relatively dispersed distribution. The coupling here is weaker. This corresponds to a confinement loss peak of approximately 4333.61 dB/cm and a resonance wavelength of about 1412.72 nm. When Δ = 0.3 μm, both polarized optical fields shift toward the D-shaped surface. The energy flow arrows show a stronger tendency to point to the coating. The

evanescent field coupling gradually increases. For the x-polarization, the loss peak rises to about 4661.29 dB/cm, and the resonance wavelength blue-shifts to approximately 1366.34 nm. Δ = 0.6 μm represents a critical displacement. The optical field distribution undergoes drastic reconstruction. The x-polarized field contracts toward the fiber core, while the concentration of the y-polarized field weakens. The energy flow directions become disordered. The coupling strength decreases from its peak value. Correspondingly, the x-polarization loss peak drops to about 1153.65 dB/cm, and the resonance wavelength blue-shifts to around 1182.08 nm. This point marks the transition where the confinement loss shifts from increasing to decreasing. When Δ increases from 0.9 μm to 1.3 μm, the optical fields in both polarization directions completely contract inward and become localized within the fiber core. The energy flow arrows no longer point toward the D-shaped coating surface. As a result, the evanescent-field coupling between the guided mode and the surface mode is strongly suppressed. The peak loss for the x-polarization falls below 445.67 dB/cm across this range. Simultaneously, the interaction between the optical field and the analyte/coating weakens significantly. This reduction lowers the effective index of the guided mode at resonance. The phase-matching condition thus shifts toward shorter wavelengths, ultimately leading to a blue shift of the resonance peak.

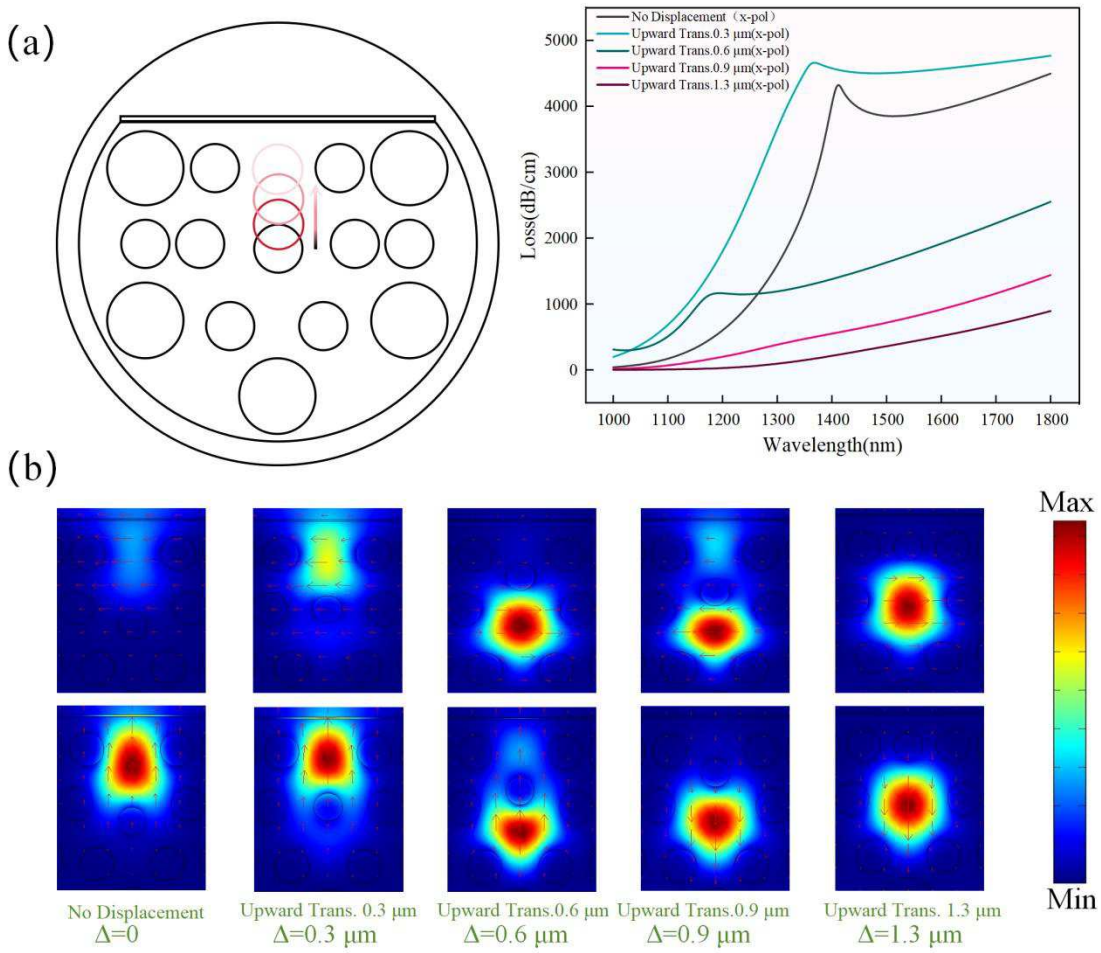


Fig. 4(a)Loss Variation of x-Polarized Core Mode with Wavelength at different displacements. (b)Electric Field Distributions of the x-Polarized Core Mode at different displacements

The center-to-center spacing between the two uppermost air holes is denoted as Λ_1. The influence of Λ_1 on the confinement loss spectrum is investigated in Fig. 5. Fig. 5(a) and 5(b) present the evolution of the optical-field energy density distributions and the energy-flow directions in the two orthogonal polarization directions as the top air-hole spacing Λ_1 varies in the D-shaped photonic crystal fiber. The color gradient from blue to red represents increasing energy density, and the red arrows indicate the direction of energy flow. In the non-displaced state, Λ_1 is 1.6 μm. The optical field in the x-polarization direction shows a teardrop-like shape. It concentrates toward the coated region on the D-shaped surface. The energy-flow arrows point to the coating surface. This indicates strong coupling between the guided mode and the surface plasmon mode. Consequently, significant energy leaks into the coating region. The corresponding confinement loss peak for the x-polarization is approximately 4319.35 dB/cm, and the resonance wavelength is about 1412.72 nm. In contrast, the optical field in the y-polarization direction is

biased toward the cladding air holes. The coupling here is weaker. As the upward displacement of the air holes increases, the spacing between them continues to decrease. The optical fields in both polarization directions gradually contract toward the interior of the fiber core. In the x-polarization, the field distribution shifts from being offset to one side and converges symmetrically toward the core center. In the y-polarization, the initially upward-concentrated field broadens and flattens gradually. The tendency of the energy-flow arrows to point toward the coating weakens significantly. At the maximum displacement, the arrows even reverse direction. As a result, the evanescent-field coupling between the guided mode and the surface mode is strongly suppressed. When Λ_1 = 1.4 μm, the confinement loss peak for the x-polarization drops to about 2506.45 dB/cm, and the resonance wavelength blue-shifts to approximately 1259.23 nm. At Λ_1 = 1.2 μm, the loss peak is about 1045.16 dB/cm, and the resonance wavelength is around 1137.14 nm. For Λ_1 values from 1.0 μm to 0.8 μm, no distinct loss peak is observed within the 1000 nm–1800 nm wavelength range. The observed trend of enhanced optical-field localization provides a clear physical explanation for the marked reduction in the loss peak as the air-hole spacing decreases. The weakened coupling results in less energy leakage. Concurrently, the interaction between the optical field and the analyte diminishes. A slight change also occurs in the effective refractive index of the guided mode. These combined effects shift the resonant phase-matching condition toward shorter wavelengths. Consequently, a blue shift in the resonance wavelength is induced.

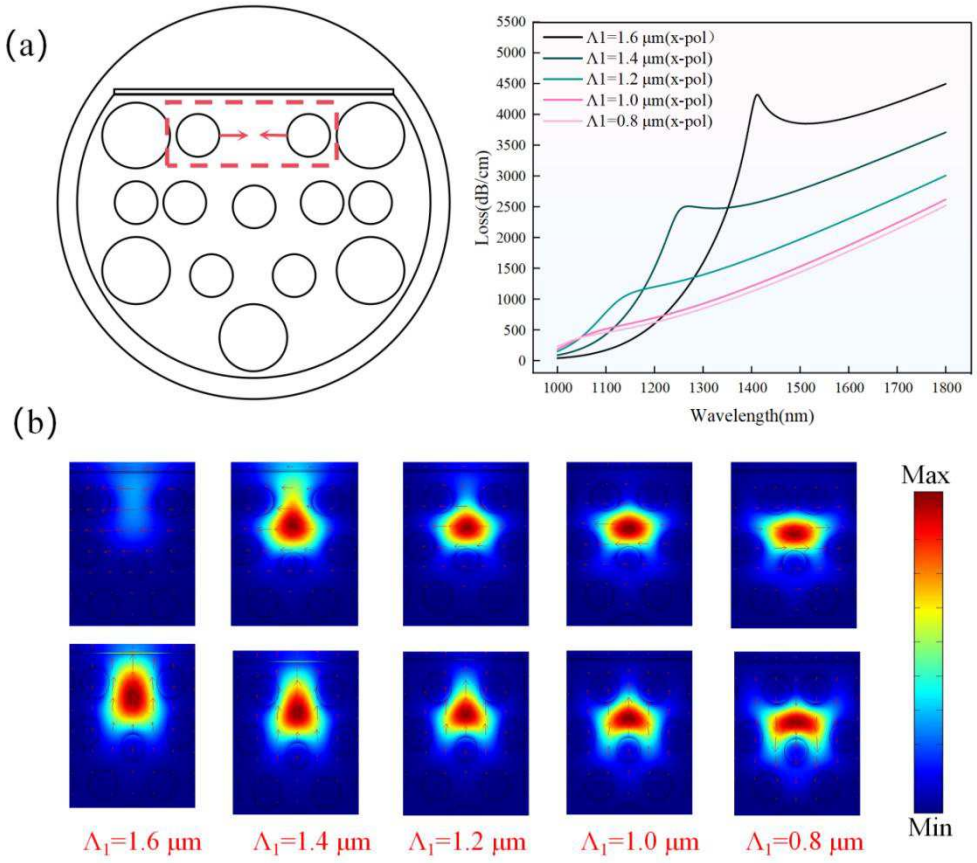


Fig. 5(a)Variation of loss for the x-Polarized core mode with wavelength at different air hole distances. (b)Electric field distributions of the x-Polarized core mode at different air hole distances.

Table 1 Refractive Index of Existing Normal and Cancerous Cells

Cancer type	Cell type	Normal cell RI	Cancerous cell RI	References
Skin	Basal	1.360	1.380	[17],[18]
Cervical	HeLa	1.368	1.392	[19],[20]
Blood	Jurkat	1.376	1.390	[21],[22]
Adrenal gland	PC-12	1.381	1.395	[17],[19]
Breast	MDA-MB-231	1.385	1.399	[18],[20]
Breast	MCF-7	1.387	1.401	[21],[22]
Prostate gland	RWPE-1	1.366±0.007	-	[23]
Prostate gland	PC-3	-	1.397±0.008	[23]
Prostate gland	DU-145	-	1.401±0.008	[23]
Lung	BEAS-2B	1.369±0.004	-	[24]
Lung	A549	-	1.385±0.005	[24]

Table 1 lists the refractive indices corresponding to currently available normal and cancerous cells. Fig. 6(a) simulates the extraction of the required cancerous and normal cells from a mouse.

Fig. 6(b) to (g) display the CL spectral profiles of six kinds of somatic cells in both healthy and cancerous states. The cancer types include: skin cancer (basal cell carcinoma), cervical cancer (HeLa cells), blood cancer (Jurkat cells), adrenal cancer (PC-12 cells), and breast cancer (MDA-MB-231 and MCF-7 cells). Compared with normal cells, all tested cancer cell samples exhibited a significant blueshift in the resonance loss peak, along with a reduction in the maximum confinement loss. Table 2 summarizes the key sensing performance metrics of the proposed biosensor. Wavelength sensitivities for breast cancer (MDA-MB-231), adrenal cancer, blood cancer, cervical cancer, and skin cancer were measured as 15,642 nm/RIU, 16,214 nm/RIU, 16,142 nm/RIU, 16,250 nm/RIU, and 16,750 nm/RIU, respectively. Among these, HeLa cells (cervical cancer) showed the largest blueshift of 392 nm, with a corresponding maximum confinement loss of approximately 5,176 dB/cm. The highest resolution achieved by the sensor was 6.36×10^{-6} RIU. Changes in the analyte's refractive index directly modulate the coupling strength between the incident light wave and the surface plasmon wave. During cell carcinogenesis, the refractive index of the cells themselves alters, leading to a shift in the resonance wavelength and a decrease in the loss peak. This observed relationship confirms that the refractive index changes caused by cell carcinogenesis can be accurately characterized by the shift of the resonance peak and the variation in loss amplitude. Therefore, the sensor enables effective detection and differentiation of the cancerous state across different cell lines.

Table 2 Comprehensive performance of the biosensor for cancer cell detection

Cell type	Wavelength Resonance (μm)	RW Shift(nm)	WS(nm/RIU)	Resolution(RIU)
Basal	(1.564-1.904)±0.01	340	16750	5.97015×10^{-6}
Hela	(1.380-1.772)±0.01	392	16250	6.15385×10^{-6}
Jurkat	(1.408-1.639)±0.01	230	16142	6.19469×10^{-6}
PC-12	(1.328-1.558)±0.01	230	16214	6.1674×10^{-6}
MDA-MB-231	(1.280-1.500)±0.01	220	15642	6.39269×10^{-6}
MCF-7	(1.240-1.460)±0.01	220	15714	6.36364×10^{-6}

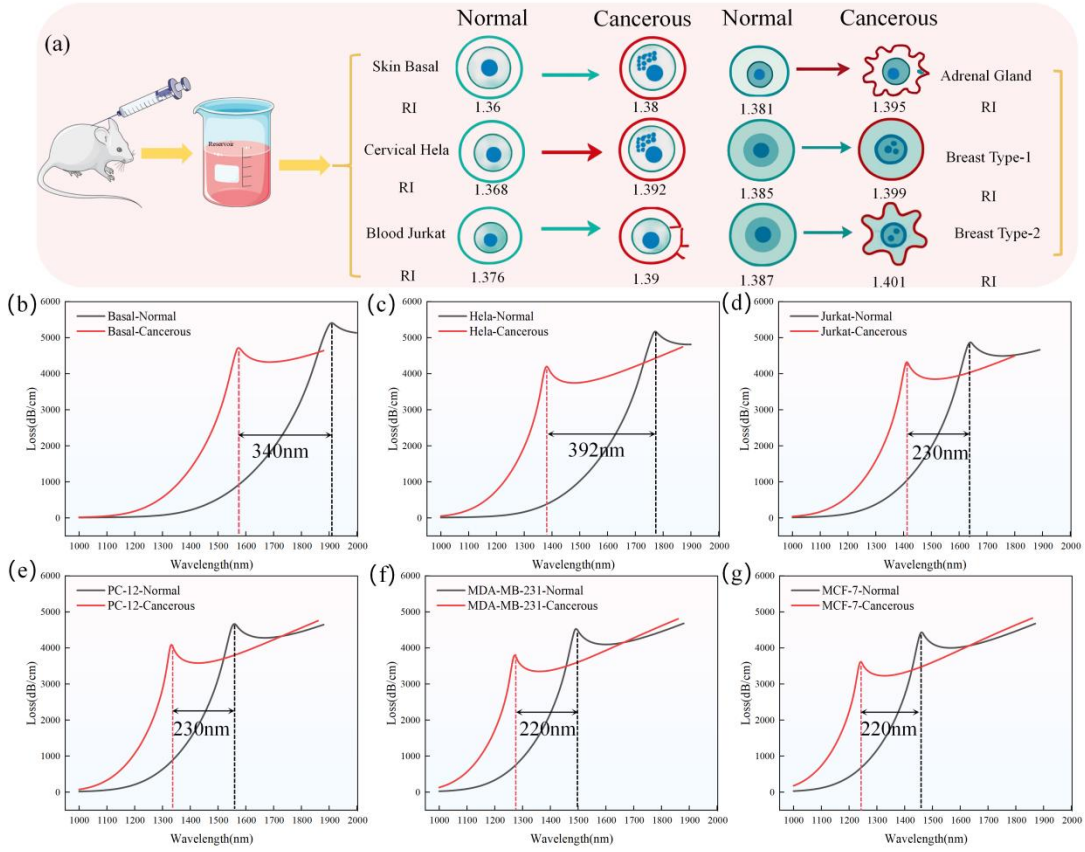


Fig. 6 (a)Refractive index of studied cells;Loss spectra of normal and cancerous cells of (b) Basal, (c) HeLa, (d)Jurkat, (e) PC-12, (f) MDA-MB-231,and (g) MCF-7

Fig. 7(a) presents the amplitude sensitivity response characteristics of the six different cell types in the near-infrared region. The amplitude sensitivity curves of all cell lines exhibit a typical valley-shaped distribution, which aligns with the response pattern of a surface plasmon resonance sensor. At the valley wavelength, the coupling strength between the core-guided mode and the surface plasmon wave reaches its maximum. This results in the highest sensitivity to changes in the cell refractive index, corresponding to the largest absolute sensitivity value. As the wavelength deviates from the valley position, the SPR coupling weakens, and the absolute sensitivity rapidly approaches zero. Notable differences exist in the valley position and peak height of the sensitivity curves among the different cell lines. HeLa cells exhibit the largest peak absolute sensitivity, approximately –553.66 RIU^{-1}, indicating the strongest detection capability. In contrast, Basal cells show the smallest peak absolute value, about –326.23 RIU^{-1}, corresponding to the relatively weakest detection performance. Meanwhile, the valley wavelengths differ markedly: HeLa and Jurkat cells have valleys near 1186 nm; PC-12, MCF-7, and MDA-B-231 cells exhibit valleys

between 1048 and 1096 nm; and Basal cells show a valley at 1292.22 nm. This variation originates from the distinct inherent refractive indices of the different cells, which are determined by their morphology, organelle composition, and intracellular protein concentration. These intrinsic differences alter the SPR resonance wavelength and coupling strength, thereby providing a fundamental basis for cell-level specific identification. Consequently, the sensor holds potential application value in fields such as early cancer diagnosis and the classification of multiple cancer-cell types. Fig. 7(b) shows the linear regression of the measured refractive indices for normal and cancerous cells, whereby the linearity of the sensor's response is quantified by the coefficient of determination. A higher R^2 value indicates better linearity of the sensor. Here, the R^2 value reaches 0.99965, which indicates that the biosensor provides an excellent continuous response for early cancer detection.

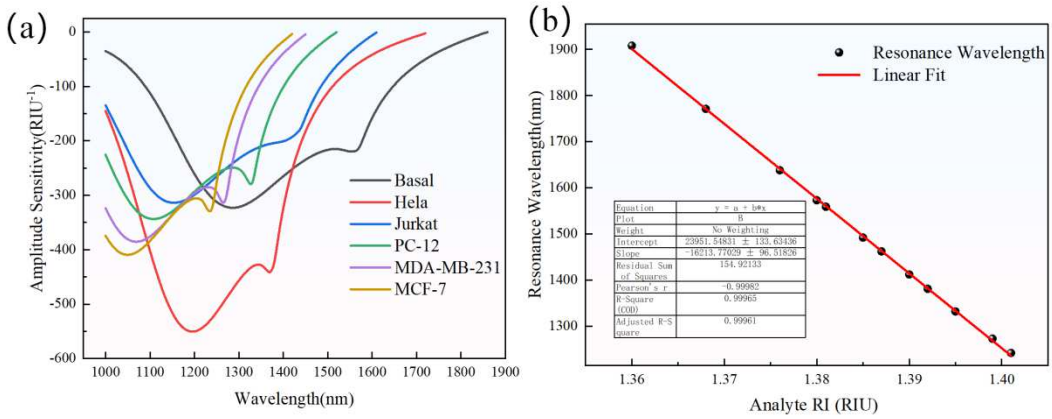


Fig. 7(a) Amplitude sensitivity for the six cancerous cells (b) Linear fitting of resonance wavelengths for RI changing in normal and cancerous cells

Table 3 Comparison of Sensitivity Among Recently Published SPR-Based Fiber Optic Sensors

Sensor type	Cell type	WS (nm/RIU)	Resolution (RIU)	Ref.
Dual Planar Metal PCF-SPR	Basal	3000	3.33×10^{-5}	[25]
	Hela	3333.33	3×10^{-5}	
	Jurkat	4285.72	2.33×10^{-5}	
	PC-12	4285.72	2.33×10^{-5}	
	MDA-MB-231	5714.28	1.75×10^{-5}	
	MCF-7	5714.28	1.75×10^{-5}	
Multi-ring Core PCF-SPR	Basal	2500	4×10^{-5}	[26]
	Hela	2916.66	3.42×10^{-5}	
	Jurkat	3571.42	2.8×10^{-5}	
	PC-12	3571.42	2.8×10^{-5}	
	MDA-MB-231	4285.71	2.3×10^{-5}	
	MCF-7	4285.71	2.3×10^{-5}	
Bowl-shaped PCF-SPR	Basal	17,500	1.5×10^{-2}	[27]

Sensor type	Cell type	WS (nm/RIU)	Resolution (RIU)	Ref.
D-shaped Planar MoO_2 PCF-SPR	Hela	10,208.33	1.4×10^{-2}	This work
	Jurkat	10,714.28	7×10^{-3}	
	PC-12	10,000	1×10^{-2}	
	MDA-MB-231	17,857.14	9.33×10^{-3}	
	MCF-7	18,071.42	8.75×10^{-3}	
	Basal	16750	5.97015×10^{-6}	
	Hela	16250	6.15385×10^{-6}	
	Jurkat	16142	6.19469×10^{-6}	
	PC-12	16214	6.1674×10^{-6}	
	MDA-MB-231	15642	6.39269×10^{-6}	
	MCF-7	15714	6.36364×10^{-6}	

In the design process of our SPR-PCF sensor, easy fabrication, high sensing performance, and wide applicability are crucial factors that determine the sensor's practicality and promotion value in cancer cell identification. The sensor exhibits excellent sensing capabilities. As shown in Table 3, compared with recently reported surface plasmon resonance sensors for cancer detection, our sensor exhibits notably enhanced sensitivity and resolution. It achieves a high spectral sensitivity of up to 16,750 nm/RIU. Moreover, the sensor attains a maximum achievable resolution of 6.39×10^{-6} RIU, surpassing that of most recently reported cancer detection biosensors. The sensor features not only a straightforward design and high performance, but also versatile applicability. Beyond its capability to detect six cancer types, the sensor is also functional for liquid detection within a specific RI range of 1.35 to 1.41.

4. Conclusion

This paper proposes and numerically verifies a D-shaped photonic crystal fiber surface plasmon resonance (PCF-SPR) sensor for early detection of somatic cell carcinogenesis. The sensor features a periodically arranged symmetric air-hole structure. A planar MoO_2 layer is deposited on the D-shaped surface as the plasmonic sensitive material. The sensing performance is systematically evaluated through finite element method (FEM) simulations. Tests on six types of cancer cells from different tissue origins—skin basal cells (Basal), cervical cancer cells (HeLa), leukemia cells (Jurkat), adrenal pheochromocytoma cells (PC-12), and breast cancer cells (MDA-MB-231 and MCF-7)—demonstrate that the designed sensor exhibits excellent spectral response characteristics. Among them, skin basal cells (Basal) achieve the highest spectral sensitivity, reaching 16,750 nm/RIU, with a corresponding detection resolution as low as 5.97×10^{-6} RIU. The spectral sensitivity for different cancer cells ranges from 15642 to

16750 nm/RIU, and the resolution varies between 5.97×10^{-6} and 6.39×10^{-6} RIU, enabling high-resolution detection of cell-level refractive index changes. Moreover, the sensor covers a refractive index detection range of 1.34 to 1.41, which meets the requirements for analyzing most biological samples. Compared to existing PCF-SPR sensors, the present design demonstrates competitive advantages in both spectral sensitivity and detection resolution. It offers a highly sensitive and reliable sensing solution for areas such as bioanalysis, early clinical cancer diagnosis, and environmental monitoring. The sensor thus holds promising potential for broad applications.

Acknowledgements

This research was supported by Natural Science Foundation of Xinjiang Uygur Autonomous Region (Grant NO. 2023D01B21, 202501A69); Basic scientific research business fees for universities in Xinjiang Uygur Autonomous Region scientific research project (Grant NO. XJEDU2023P140); the Xinjiang Institute of Engineering (Project NO. 2024xgy192605); National Innovation and Entrepreneurship Training Program for College Students (Grant No. 202510994004); Innovation and Entrepreneurship Training Program for College Students of Xinjiang Uygur Autonomous Region (Grant No.S202510994029); the Basic Research Program of Shanxi Province (NO.202303021222211).

Reference

[1] Mangayarkarasi S, et al. (2025) Enhancing cancer screening and early diagnosis in India: overcoming challenges and leveraging emerging technologies. Cureus 17(2):e34057. PMC11902917.

[2] Tajima K, et al. (2003) Expression of cancer/testis (CT) antigens in lung cancer. Lung Cancer 42(1):23-33.

[3] Glunde K, Bhujwalla ZM (2011) Metabolic tumor imaging using magnetic resonance spectroscopy. Semin Oncol 38(1):26-41.4.

[4] Furusawa Y, et al. (2012) DNA double-strand breaks induced by cavitational mechanical effects of ultrasound in cancer cell lines. PLoS One 7 (1):e29012.

[5] Rifat AA, et al. (2018) Highly sensitive selectively coated photonic crystal fiber-based plasmonic sensor. Opt Lett 43 (4):891–894.

[6] Malakar T, Amina N N, Lalin N S, et al. (2026) Optimized single-core PCF-based SPR biosensor for high-performance early-stage multi-cancer detection. arXiv arXiv:2510.17283v3.

[7] Nagavel B, Dagar H, Krishnan P (2025) High-performance dual-core bilateral surface optimized PCF SPR biosensor for early detection of six distinct cancer cells. Plasmonics 20:4799–4809.

[8] Ibrahimi K M, Kumar R, Pakhira W (2024) C-grooved dual-core PCF SPR biosensor with graphene/au coating for enhanced early cancer cell detection. Appl Phys A-Mater Sci Process 130:439.

[9] Ibrahimi K M, Kumar R, Pakhira W (2023) Enhance the design and performance analysis of a highly sensitive twin-core PCF SPR biosensor with gold plating for the early detection of cancer cells. Plasmonics 18:995–1006.

[10] Khodatars Dashtmian M R, Fallahi V, Seifouri M, et al. (2025) Gold nanowire-enhanced SPR-PCF biosensor for high-throughput cancer cell detection in near-infrared. Plasmonics.

[11] Islam N, Arif M F H, Abu Yousuf M, Asaduzzaman S (2023) Highly sensitive open channel based PCF-SPR sensor for analyte refractive index sensing. Results Phys 46:106266.

[12] Dong J, Zhang S, Zhao G, Peng M, Yang Y, Zhua H, Wang Z, Lan B (2024) Ultra high sensitivity D-type photonic crystal fiber sensor deposited with MoO_2 nanofilm. Optical Materials 152:115483.

[13] Liu Y C, Li S G, Chen H L, Li J S, Zhang W X, Wang M Y (2020) Surface plasmon resonance induced high sensitivity temperature and refractive index sensor based on evanescent field enhanced photonic crystal fiber. J Lightwave Technol 38 (4):919–928.

[14] Guo Y, Li J S, Li S G, Liu Y D, Zhang S H, Wang J, Wang S, Zhang W X, Cheng T L, Hao R (2020) Dual-polarized optical sensing of microstructure fiber with pentagonal-lattice based on surface plasmon resonance in the near-IR spectrum. Optik 202:163671.

[15] Li T S, Zhu L Q, Yang X C, Lou X P, Yu L D (2020) A refractive index sensor based on H-shaped photonic crystal fibers coated with Ag-graphene layers. Sensors 20 (3):741.

[16] Chu S D, Nakkeeran K, Abobaker A M, Aphale S S, Babu P R, Senthilnathan K (2019) Design and analysis of surface-plasmon resonance-based photonic quasi-crystal fiber biosensor for high refractive-index liquid analytes. IEEE J Sel Top Quantum Electron 25 (2):1–9.

[17] Singh S, Kumar R, Chaudhary B, et al. (2025) Gold immobilized SPR-enhanced PCF biosensor for detection of cancer cells: a numerical simulation. Plasmonics 20:3535–3544. https://doi.org/10.1007/s11468-024-02578-w.

[18] Sardar M R, Faisal M (2024) Dual-core dual-polished PCF-SPR sensor for cancer cell detection. IEEE Sensors Journal 24(7):9843–9854. doi:10.1109/JSEN.2024.3358173.

[19] Majeed M F, Ahmad A K (2024) Design and analysis of a dual-core PCF biosensor based on SPR for cancerous cells detection. Opt Quant Electron 56:1030. https://doi.org/10.1007/s11082-024-06566-6.

[20] B N, Dagar H, Krishnan P (2025) High-performance dual-core bilateral surface optimized PCF SPR biosensor for early detection of six distinct cancer cells. Plasmonics 20:4799–4809. https://doi.org/10.1007/s11468-024-02661-2.

[21] Yasli A (2021) Cancer detection with surface plasmon resonance-based photonic crystal fiber biosensor. Plasmonics 16(5):1605–1612.

[22] Parvin T, Ahmed K, Alatwi A M, Rashed A N Z (2021) Differential optical absorption spectroscopy-based refractive index sensor for cancer cell detection. Opt Rev 28(1):134–143.

[23] Kim J, Lee S, Park H, et al. (2020) Cellular refractive index comparison of various prostate cancer and noncancerous cell lines via photonic-crystal biosensor. Sensors 20(11):3145. doi:10.3390/s20113145.

[24] Schürmann C, Cojoc G, Ferrari A, et al. (2019) Quantitative phase imaging of lung cancer cells for label-free identification. Optics Express 27(19):28752–28765. doi:10.1364/OE.27.028752.

[25] Nagavel B, Dagar H, Krishnan P (2025) High-performance dual-core bilateral surface optimized PCF SPR biosensor for early detection of six distinct cancer cells. Plasmonics 20:4799–4809.

[26] Ibrahimi K M, Kumar R, Pakhira W (2023) Enhance the design and performance analysis of a highly sensitive twin-core PCF SPR biosensor with gold plating for the early detection of cancer cells. Plasmonics 18:995–1006.

[27] Jabin M A, Ahmed K, Rana M J, Paul B K, Islam M, Vigneswaran D, Uddin M S (2019) Surface plasmon resonance based titanium coated biosensor for cancer cell detection. IEEE Photon J 11(4):1–10.